

Geometry without Position? When Positional Embeddings Help and Hurt Spatial Reasoning

Jian Shi¹ Michael Birsak¹ Wenqing Cui¹ Zhenyu Li¹ Peter Wonka¹

Abstract

This paper revisits the role of positional embeddings (PEs) within vision transformers (ViTs) from a geometric perspective. We show that PEs are not mere token indices but effectively function as geometric priors that shape the spatial structure of the representation. We introduce token-level diagnostics that measure how multi-view geometric consistency in ViT representation depends on consistent PEs. Through extensive experiments on 14 foundation ViT models, we reveal how PEs influence multi-view geometry and spatial reasoning. Our findings clarify the role of PEs as a causal mechanism that governs spatial structure in ViT representations. Our code is provided in <https://github.com/shijianjian/vit-geometry-probes>

1. Introduction

Vision Transformers (ViTs) (Dosovitskiy et al., 2021) have revolutionized visual representation learning yet their ability to reason about geometry remains insufficiently understood. While the self-attention mechanism enables flexible and long-range dependencies, it is inherently permutation-invariant and lacks any explicit spatial structure. Consequently, ViTs rely on positional embeddings (PEs) to encode the “where” of image patches to introduce coordinates for each token.

Early analyses have offered mixed insights. Raghu *et al.* (Raghu et al., 2021) reported that standard ViTs (trained with a CLS token) are likely to retain strong local spatial representations within their deep layers, suggesting that geometric cues can emerge even without convolution. However, later studies such as Probe3D (El Banani et al., 2024) revealed that large-scale foundation models still struggle with

¹King Abdullah University of Science and Technology, Thuwal, Saudi Arabia. Correspondence to: Jian Shi <jian.shi@kaust.edu.sa>, Peter Wonka < peter.wonka@kaust.edu.sa>.

multi-view correspondence and suffer under large viewpoint changes, indicating a lack of geometric generalization. Notably, while single-view approaches such as DepthAnything (Yang et al., 2024) benefit directly from pretrained DINOv2 (Oquab et al., 2024) representations, multi-view methods like VGGT (Wang et al., 2025a) and π^3 (Wang et al., 2025b) typically retrain DINO-based backbones to achieve cross-view consistency. This contrast suggests that ViTs might encode geometry in a view-dependent manner, rather than being intrinsically tied to visual content alone.

A natural hypothesis is that such behavior arises from the design of PEs. Because attention lacks intrinsic spatial bias, ViTs depend on PEs to impose spatial order. Various forms of PEs have been proposed for both 2D and 3D understanding, including absolute coordinate embeddings (Carion et al., 2020; Chu et al., 2023; Touvron et al., 2021), relative positional biases (Li et al., 2021b), and rotary encodings for angular consistency (Su et al., 2024). While PEs are known to stabilize training and improve recognition performance (Carion et al., 2020; Chu et al., 2023; Touvron et al., 2021), they have also been observed to degrade geometric alignment and correspondence accuracy (Sun et al., 2021; Li et al., 2021b). For example, DeiT (Touvron et al., 2021) demonstrated that inappropriate PE schemes tend to overfit to spatial layouts rather than learn transferable geometric features. LoFTR (Sun et al., 2021) observed that adopting a DETR-style (Carion et al., 2020) architecture with PEs at every layer led to a decline in feature matching performance, implying that excessive positional bias can hinder correspondence learning. Li *et al.* (Li et al., 2021b) observed that the choice between absolute and relative PEs can drastically affect convergence and localization accuracy. Recent works like PE-Fields (Bai et al., 2025) further reveal that positional fields can even govern volumetric reasoning in generative settings, suggesting that PEs play a deeper role in geometric reasoning than previously assumed.

Prior studies establish that PEs are essential for spatial awareness, yet their precise role in shaping geometric structure remains unclear. Thus, we ask:

To what extent do positional embeddings determine the geometric structure of visual representations, and under what conditions do they facilitate

Table 1. Comparison of representative foundation ViT architectures and vision encoders. We categorize by training paradigm (SUP = supervised, SSL = self-supervised learning, VLM = vision–language modeling, MIM = masked image modeling), dataset scale, and positional encoding (PE) strategy.

Model	Training Objective	Data	Scale	PE Strategy
ViT-B/16 (Dosovitskiy et al., 2021)	Classification (SUP)	JFT-300M	303M	Absolute
DeiT (Touvron et al., 2021)	Classification + distillation (SUP, SSL)	ImageNet-1k	1.28M	Absolute
DINO (Zhang et al., 2023a)	Self-distillation (SSL)	ImageNet-1k	1.28M	Absolute
DINOv2 (Oquab et al., 2024)	Self-distill. + register tokens (SSL)	LVD (Curated multi-source images)	142M	Absolute
DINOv3 (Siméoni et al., 2025)	Self-distillation (SSL)	Web-scale curated images	~1.7B	Rotary
BEiT (Bao et al., 2022)	Masked image modeling (MIM)	ImageNet-21k	14M	Relative
Data2Vec-Vision (Baevski et al., 2022)	Latent prediction (SSL)	ImageNet-1k	1.28M	Relative
CLIP (Radford et al., 2021)	Contrastive (VLM)	Web image–text pairs	400M	Absolute
I-JEPA (Assran et al., 2023)	Context prediction (SSL)	ImageNet-1k	1.28M	Absolute
SAM (Kirillov et al., 2023)	Segmentation (SUP)	SA-1B	11M imgs / 1.1B masks	Absolute
SigLIP2 (Tschannen et al., 2025)	Multi-Stage (SUP, SSL, MIM, VLM)	WebLI	~10B	Absolute
MLCD (An et al., 2024)	Contrastive distillation (SSL)	LAION-400M	~400M	Rotary
Swin Transformer (Liu et al., 2021b)	Classification (SUP)	ImageNet-1k	1.28M	Relative
SwinV2 (Liu et al., 2021a)	Detection / Segmentation (SUP)	ImageNet-22k + COCO	22M + 118k	Relative

or hinder spatial reasoning?

We investigate this through a direct, token-level analysis of 14 foundation ViTs spanning diverse PE strategies (Table 1). In this work, we define geometric structure as the preservation of relative spatial relations between tokens under changes in viewpoint. Unlike most works (El Banani et al., 2024; Chen et al., 2025) indirectly evaluated PEs through downstream tasks, our approach explicitly decouples visual content from positional structure at the token level.

This work provides a systematic analysis of the geometric role of PEs in ViTs. Rather than treating PEs as auxiliary coordinates, our key perspective is to view PEs as inducing an *implicit spatial kernel* that governs how tokens interact with visual content as a function of position. Notably, ViT representation encodes spatial relations relative to the model’s own viewpoint defined by PEs. Through controlled experiments that decouple visual content and PEs, we demonstrate that geometric structure across views depends primarily on the consistency of PEs, rather than on visual content alone. We further show that correspondence degradation under viewpoint change can be largely reversed by restoring the PE alignment. These findings reframe PEs as a causal mechanism underlying spatial reasoning in ViTs.

2. Related Work

2.1. Geometry and Locality in ViTs

A central difficulty in modern vision representation learning is balancing local geometric fidelity and global semantic abstraction. Chen et al. (Chen et al., 2023) directly investigates the representation trade-off between local and global features and shows that many models need to balance both for dense tasks. Empirically, though semantically rich, deeper layers tend to lose local structure and positional distinctiveness (Park & Kim, 2022; Yuan et al., 2021). Conversely, architectures emphasizing locality (Li et al., 2021a;

Chen et al., 2022; Tu et al., 2022) maintain sharper geometric features but lack semantic robustness under large view or appearance changes. Self-supervised foundation models illustrate this trade-off in distinct forms, such as DINOv2 (Oquab et al., 2024) exhibit weakened geometric correspondence (El Banani et al., 2024), while predictive models like I-JEPA (Assran et al., 2023) further emphasize semantic abstraction at the expense of spatial precision. At the time of this study, even state-of-the-art foundation models such as DINOv3 (Siméoni et al., 2025) explicitly state the persistent local–global dilemma, where improved global consistency comes at the expense of local spatial fidelity. In this work, we revisit the local–global feature balancing from the perspective of positional encoding, revealing how PEs shape the local–global feature trade-off.

2.2. The Role of Positional Embedding

Transformers are permutation-invariant and thus require explicit spatial priors. PEs provide such cues by encoding the 2D layout of image patches. Mainstream positional encoding methods include absolute (Carion et al., 2020), relative (Wu et al., 2021), and rotary (Su et al., 2024). Notably, a series of studies reported that the choice of positional encoding methods can heavily affect the performance on tasks that demand spatial reasoning. DETR (Carion et al., 2020) first demonstrated that omitting PEs causes a sharp drop in detection accuracy, as the model loses absolute localization cues. Similarly, CPVT (Chu et al., 2023) and DeiT (Touvron et al., 2021) reported that dropping or mismatching PEs reduces classification accuracy and harms robustness to input resolution changes, indicating that absolute spatial priors improve model generalization. For correspondence-driven tasks, explicit positional cues are even more critical. LoFTR (Sun et al., 2021) uses 2D positional encodings in its Local Feature Transformer and notes that positional information, together with global receptive fields, is crucial for obtaining high-quality matches. STTR (Li et al., 2021b)

further shows that relative positional information is necessary for resolving ambiguity in textureless regions and for producing stable disparity patterns. Recent 3D transformer models (Liu et al., 2022; Li et al., 2021b) introduce disparity- or depth-aware PEs to capture spatial structure across multiple views. Overall, PEs remain indispensable for preserving geometric coherence, even though their geometric effects remain underexplored. This work provides a token-level analysis of the impact of PEs.

3. PEs as Spatial Kernels

Transformers process a sequence of tokens without any built-in notion of spatial order. For image inputs, this means that tokens corresponding to local patches are treated as unordered elements unless additional positional cues are provided. To encode spatial structure, ViTs introduce PEs that supply information about the location of each token. Let $x_i \in \mathbb{R}^d$ denote the feature of the i -th token. The query and key projections are given by:

$$q_i = W_Q x_i, \quad k_j = W_K x_j,$$

and the raw attention logits (before softmax) are:

$$\alpha_{ij} = \frac{1}{\sqrt{d}} q_i^\top k_j. \quad (1)$$

Note that this representation has not added any positional signal yet. Depending on how the positional signal is formulated, three main variants are commonly used: *absolute*, *relative*, and *rotary* encodings.

3.1. Background: Absolute, Relative, and Rotary PEs

Absolute positional encodings. Each token receives a unique embedding that encodes its absolute position $p_i = f(i)$ on the image grid, such that:

$$q_i = W_Q(x_i + p_i), \quad k_j = W_K(x_j + p_j), \quad (2)$$

Common formulations include sinusoidal encodings (Vaswani et al., 2017; Dosovitskiy et al., 2021) and learned embeddings (Touvron et al., 2021). By encoding absolute coordinates, absolute PEs are not translation-invariant, leading to position-dependent attention patterns.

Relative positional encodings. Relative encodings (Shaw et al., 2018; He et al., 2021; Press et al., 2022) do not modify tokens. Position is directly injected in the logits with a function $b(\Delta_{ij})$ of the displacement $\Delta_{ij} = j - i$:

$$\alpha_{ij} = \frac{1}{\sqrt{d}} q_i^\top k_j + b(\Delta_{ij}), \quad (3)$$

that depends only on relative offset rather than absolute location. This enhances translation invariance and stability across resolutions.

Rotary positional encodings (RoPE). Rotary PEs (Su et al., 2024) inject position by rotating queries and keys in a complex-valued space. Given the projected queries and keys q_i and k_j , RoPE assigns each position i an angle θ_i derived from fixed sinusoidal functions, and applies

$$q_i \leftarrow \mathcal{R}_{\theta_i}(q_i), \quad k_j \leftarrow \mathcal{R}_{\theta_j}(k_j),$$

Since rotations compose additively, the attention logit becomes: This results in dot-products of the form:

$$q_i^\top k_j = q_i^\top \mathcal{R}_{\theta_j - \theta_i}(k_j), \quad (4)$$

which depends only on the relative phase $\theta_j - \theta_i$, effectively encoding angular or offset-based relationships in a multiplicative manner.

3.2. A Kernel Interpretation of PEs

We provide an interpretive decomposition of the attention mechanism that clarifies how PEs influence spatial interactions between tokens. We emphasize that this analysis does not introduce a new attention formulation, nor does it claim a formal equivalence between attention and kernel methods. Instead, it offers a conceptual lens for understanding how different positional encoding schemes impose structured spatial priors on token interactions.

Absolute & Relative Positional Encoding (RPE). We begin from the standard attention logit formulation introduced in Eq. (1). Following (Press et al., 2022; Li et al., 2021b), we expand the dot-product attention with additive positional embeddings into four components:

$$\alpha_{ij} = \underbrace{\frac{1}{\sqrt{d}} x_i^\top W_Q^\top W_K x_j}_{\text{content-content}} + \underbrace{\frac{1}{\sqrt{d}} x_i^\top W_Q^\top W_K p_j}_{\text{content} \rightarrow \text{position}} + \underbrace{\frac{1}{\sqrt{d}} p_i^\top W_Q^\top W_K x_j}_{\text{position} \rightarrow \text{content}} + \underbrace{\frac{1}{\sqrt{d}} p_i^\top W_Q^\top W_K p_j}_{\text{position-position}}. \quad (5)$$

This decomposition separates content-driven similarity from positional contributions. The first term encodes content-based similarity (semantic affinity between tokens), while the remaining three terms inject spatial bias through positional embeddings. The final term depends solely on the positional embeddings and the learned projection matrices, and therefore captures a purely positional interaction.

To make this effect explicit, we consider the expected contribution of the attention logits under mild and commonly used assumptions. Specifically, in pretrained ViTs, features are normalized by pre-LayerNorm and exhibit approximately zero mean ($\mathbb{E}[x] = 0$) across tokens and images. Under this setting, cross terms involving both content and position are typically smaller in expectation than the purely positional interaction. While these assumptions are not exact and need

not hold for every token or layer, they provide a useful approximation for analyzing the dominant spatial bias induced by positional encodings. Under this approximation, the expected attention logit can be written as

$$\mathbb{E}[\alpha_{ij}] \propto p_i^\top M p_j + g(\Delta_{ij}), \quad (6)$$

where $M = W_Q^\top W_K$ represents a learned bilinear form and g is any explicit relative bias. Equation (6) reveals that positional encodings induce an implicit spatial interaction pattern between tokens.

Rotary positional encodings (RoPE). Unlike additive positional embeddings, RoPE does not introduce explicit positional vectors. Instead, it modulates the interaction between queries and keys through multiplicative phase shifts. For each each query or key vector $q_i, k_i \in \mathbb{R}^d$ (e.g. $d = 768$), RoPE applies independent 2D rotations to each pair of adjacent feature dimensions:

$$(q_{2b-1}, q_{2b}) \quad \text{for } b = 1, \dots, \frac{d}{2}. \quad (7)$$

Referring to Equation (4), for one 2D feature pair (q_{2b-1}, q_{2b}) and (k_{2b-1}, k_{2b}) , we have:

$$\alpha_{ij}^b = [q_{2b-1} \ q_{2b}] \mathcal{R}_{(i-j)\theta_b} \begin{bmatrix} k_{2b-1} \\ k_{2b} \end{bmatrix}. \quad (8)$$

Expanding to:

$$\begin{aligned} \alpha_{ij}^b = & (q_{2b-1} k_{2b-1} + q_{2b} k_{2b}) \cos(\Delta\phi_{ij}^b) \\ & + (q_{2b} k_{2b-1} - q_{2b-1} k_{2b}) \sin(\Delta\phi_{ij}^b), \end{aligned} \quad (9)$$

where we use $\Delta\phi_{ij}^b = (j-i)\theta_b$ to denote the difference in rotation angles. Under the zero-mean expectation, we assume both the $2b-1$ -th and $2b$ -th components of q and k share the same expected correlation value λ_b . Therefore, by assuming the expected covariance between corresponding query-key components is the same $\mathbb{E}[q_{2b-1} k_{2b-1}] = \mathbb{E}[q_{2b} k_{2b}] = \lambda_b$ and others= 0, we get:

$$\mathbb{E}[\alpha_{ij}^b] = \lambda_b \cos(\Delta\phi_{ij}^b). \quad (10)$$

Hence, the expected dot product between a rotated query-key pair depends solely on the relative phase $(\theta_i - \theta_j)$, demonstrating that RoPE encodes a cosine-shaped positional kernel. This expression indicates that, in expectation, the interaction strength between tokens depends on a cosine function of their relative positional offset.

The PE-induced Kernel. We refer to the mentioned interactions as *implicit spatial kernels*, not in the sense of fixed or explicitly defined kernel functions, but as the learned positional prior that governs how strongly tokens at different spatial locations attend to one another. This kernel interpretation is not meant as an exact equivalence, but as

a diagnostic abstraction. In absolute encodings, this kernel takes the form of a non-stationary bilinear Gram matrix $p_i^\top M p_j$, while in relative and rotary encodings, it becomes a stationary or phase-stationary kernel depending on relative displacement. It raises the possibility that ViT representations can be factorized into content- and position-dependent components.

Under this interpretation, PEs do not merely annotate token locations. Instead, they induce a learned spatial interaction prior that structures the representation space itself. The resulting representation is then defined with respect to this PE kernel. Kernel visualizations are provided in supplementary.

4. Content vs. Position: When Geometry Breaks in ViTs

Spatially consistent feature representations are often assumed to arise from visual content similarities. However, as formalized in Equations (5) and (9), token representations inherit a PE-induced kernel, rather than being purely content-driven. This coupling is important for multi-view geometry. Prior work shows that PEs can degrade cross-view alignment (Sun et al., 2021; El Banani et al., 2024), but the underlying reason is still under-explored. Thus, we design multi-view correspondence experiments to isolate PE’s effects. Notably, multi-view correspondence serves as a stress test for spatial consistency, rather than as the primary task of interest.

4.1. ViT Representations Fail Under Identical Content

We consider overlapping image crops as a minimal correspondence setting, which preserves image content while selectively perturbs PEs.

Setup. Given an image \mathbf{I} , we generate two overlapping crops, \mathbf{I}_1 and \mathbf{I}_2 , such that the overlapping region contains identical pixels but with misaligned PE kernels. Since the overlapping regions contain identical content, any similarity

Table 2. Spatial anchoring fails despite identical content under overlapping crops. Cross-view token similarity is evaluated within the overlapping region of two crops that share identical pixel content. Increasing crop offset induces positional misalignment and leads to a pronounced drop in correspondence.

	PE	$\Delta x = 1$	$\Delta x = 2$	$\Delta x = 3$
DINO	Abs.	0.9782	0.9765	0.9627
DINOv2	Abs.	0.6775	0.5760	0.5272
DINOv3	Rot.	0.9261	0.7377	0.6564
MLCD	Rot.	0.8209	0.7345	0.6786
I-JEPA	Abs.	0.7318	0.7283	0.7280
DeiT	Abs.	0.8184	0.8003	0.7947
SigLIP2	Abs.	0.6468	0.6920	0.6872
BEiT	Rel.	0.9998	0.9997	0.9997
Data2Vec	Rel.	0.9850	0.9678	0.9469
ViT	Abs.	0.7913	0.7737	0.7416
CLIP	Abs.	0.6758	0.6665	0.6711
SAM	Abs.	0.9969	0.9945	0.9921
Swin	Rel.	0.6928	0.6928	0.5899

When Positional Embeddings Help and Hurt Spatial Reasoning

Table 3. Stereo probing results at 448x resolution. Removing and shuffling positional embeddings (**Zeroed Out PE** and **Shuffled PE**) disrupts spatial correspondence, leading to larger disparity errors (EPE↑) and weaker spatial anchoring. Though visually uninterpretable (see supplementary), **pairwise shuffled PE** generally preserve correspondence for absolute PEs. Conversely, models with intact positional encodings (**Vanilla PE**) retain sharper geometric priors, achieving lower EPE and higher recall (R@k).

Model	Vanilla PE			Zeroed Out PE			Pairwise Shuffled PE			Shuffled PE		
	EPE↓	R@1↑	R@5↑	EPE↓	R@1↑	R@5↑	EPE↓	R@1↑	R@5↑	EPE↓	R@1↑	R@5↑
DINO	11.40	0.146	0.560	24.21	0.126	0.477	8.35	0.146	0.564	63.86	0.032	0.129
DINOv2	12.64	0.131	0.515	38.08	0.087	0.315	9.93	0.143	0.551	65.29	0.028	0.114
DINOv3	11.66	0.129	0.474	51.89	0.080	0.293	60.36	0.034	0.133	60.51	0.034	0.133
I-JEPA	9.90	0.151	0.561	44.97	0.088	0.321	8.69	0.148	0.562	67.37	0.028	0.112
DEiT	14.69	0.152	0.553	26.22	0.122	0.436	10.42	0.152	0.562	66.87	0.027	0.111
SigLIP2	11.04	0.141	0.519	38.99	0.088	0.312	8.35	0.152	0.562	65.71	0.029	0.116
BeiT	28.98	0.143	0.531	46.31	0.115	0.441	42.72	0.136	0.509	60.57	0.054	0.210
Data2Vec	17.55	0.153	0.564	39.64	0.112	0.424	29.02	0.143	0.525	62.87	0.052	0.194
MLCD	23.25	0.112	0.416	38.36	0.086	0.314	59.36	0.033	0.133	59.39	0.033	0.134
SAM	19.67	0.153	0.569	47.07	0.156	0.574	9.56	0.152	0.534	58.10	0.026	0.107
CLIP	21.39	0.148	0.531	53.80	0.081	0.290	19.24	0.145	0.535	66.75	0.026	0.106
Swin	30.87	0.087	0.331	34.89	0.088	0.323	40.18	0.077	0.279	52.01	0.056	0.213
SwinV2	27.53	0.095	0.360	33.99	0.088	0.329	11.74	0.145	0.554	44.72	0.065	0.240

degradation cannot be attributed to semantic variation.

We use the test split from Imagenette (Howard, 2019) and measure the cosine similarity of cross-view tokens on the overlapping regions. We repeat this analysis for increasing horizontal displacements $\Delta x \in \{1, 2, 3\}$, which induce progressively larger positional reference mismatch.

Results. As shown in Table 2, we observe a pronounced degradation in correspondence as the horizontal offset between crops increases, despite identical visual input. This occurs consistently across models with different PEs, suggesting that it is not an artifact of a particular architecture or positional encoding scheme. Given identical visual content in the overlapping regions, any degradation in cross-view spatial anchoring must arise from mismatched PEs rather than insufficient visual representation.

4.2. Positional Mismatch in Stereo Correspondence

Overlapping crops provide a token-level probe of PE mismatch. In addition, previous studies (Oquab et al., 2024; Amir et al., 2021) show that ViT tokens preserve spatial locality and positional structure also at patch-level granularity. Yet, sub-patch correspondence behavior across views has not been systematically examined. We therefore design geometric correspondence experiments using a stereo dataset whose disparities predominantly lie within the size of a single token. This setup provides a direct and interpretable measure of whether fine positional anchoring at the sub-patch scale is preserved across views. When anchoring is preserved, correspondence remains localized, resulting in sub-patch end-point errors (EPE). Conversely, when anchoring is weakened or mismatched, correspondence peaks drift away, leading to larger EPE.

Setup Given left and right tokens $\mathbf{F}_L, \mathbf{F}_R$ extracted from a rectified stereo pair, we compute a 4D correlation volume to measure pairwise feature similarity across views. The construction of the 4D correlation volume is conceptually

related to the correlation layers employed in optical flow estimation (Dosovitskiy et al., 2015; Sun et al., 2018; Teed & Deng, 2020). For each token location (i, j) in \mathbf{F}_L , we evaluate its correspondence along the epipolar line in the right view with a *soft-argmax* operation. We evaluate on four PE settings, including 1) vanilla PE, 2) zero out PE, 3) shuffled PE, and 4) pairwise shuffled PE. Zeroed-out PE removes positional information entirely. Shuffled variants preserve positional information but assign it inconsistently, whereas pairwise shuffled maintains the same PE permutations across views. Technical details for 4D correlation volume and PE probing variants are provided in the supplementary.

We use stereo pairs from the Spring (Mehl et al., 2023) dataset at 448×448 resolution. We sample the first ten pairs from each scene, resulting in a total of 370 pairs. Left and right tokens are resized to 448×448 for the 4D correlation volume construction. We compute EPE and Recall@ n and $n \in \{1, 5\}$ to quantify geometric correspondence accuracy. Lower EPE indicates higher correspondence precision, while higher Recall@ n reflects stronger epipolar consistency.

Results. We present quantitative and qualitative results in Table 3 and Figure 1, respectively. Quantitative metrics are derived from bilinearly upsampled tokens, whereas AnyUp (Wimmer et al., 2025) is used for producing semantically meaningful visualizations. Additional visualization for shuffled PEs are provided in the supplementary.

With vanilla PEs, almost all models (except BeiT, discussion provided in supplementary) attain sub-patch correspondence, with mean EPE below the effective patch size. Epipolar peak responses exhibit sharp peaks (except BeiT and SAM), indicating that the PE-induced kernel provides spatial anchoring. However, zeroing out or shuffling PEs can significantly collapse the correspondence. EPE typically increases beyond one patch size, Recall@ n drops substantially, and epipolar responses become diffuse or unstable.

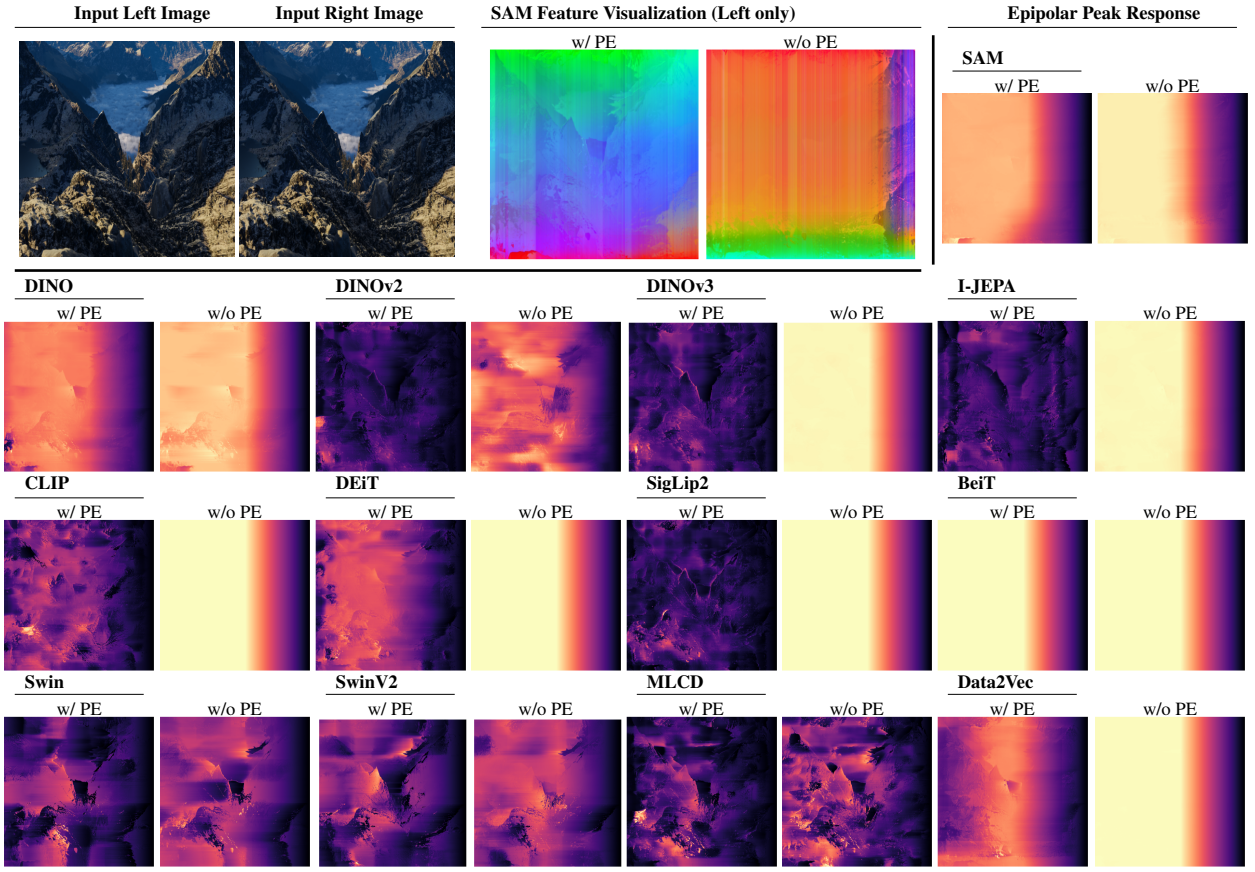


Figure 1. Epipolar peak response visualization. Top-left: an example stereo pair and the corresponding SAM feature maps with and without PEs. Removing PE substantially weakens the spatial anchoring in the token representations. **Remaining panels** show the epipolar peak responses for each evaluated model. With PEs enabled, nearly all models (except BEiT) exhibit well-localized epipolar peaks, indicating preserved spatial anchoring. After removing PEs, epipolar responses vanish for most architectures, revealing that spatial anchoring degrades without positional signals. We use AnyUp (Wimmer et al., 2025) to obtain semantically meaningful feature visualizations. Please refer to the supplementary for (pairwise) shuffled PE visualizations.

Interestingly, though visually uninterpretable (see supplementary), pairwise shuffling largely remains correspondence for the models with absolute PEs. This behavior indicates that, for absolute PEs, geometric correspondence depends primarily on the consistency of PEs across views rather than on their precise spatial correctness.

4.3. On The Role of PE Consistency

We observe that pairwise shuffling, where both views share the same permutation of PEs, does not always degrade correspondence as severely as independent random shuffling. Although the resulting spatial organization can be distorted or visually corrupted (see supplementary), a permuted but shared PE frame allows tokens to remain partially anchored across views from token representations, especially with absolute PEs. In contrast, independently shuffled PEs across views collapse the entire spatial anchoring.

A natural interpretation is that, geometric alignment in ViT representations does not solely depend on the visual content, but also on the consistency of PEs across views.

§ **Positional embeddings go beyond providing coordinates.** They contribute substantially to the spatial organization of ViT representations.

§ **Spatial scaffolding requires positional consistency.** With consistent PEs, cross-view tokens are conditioned on the same PE kernel, allowing spatial relationships to be preserved.

5. Consistent PEs for Multi-View Geometry

Now, we identify inconsistent PEs as a primary cause of geometric degradation in ViTs. We next study approaches for reconciling the inconsistency for multi-view geometry.

5.1. Restoring PE Consistency via Token Re-Indexing

In representation learning, geometric correspondence is typically attributed to shared visual content across views. However, the representations in ViTs are anchored to an internal positional reference frame. A natural question follows:

How does internal positional reference frame across views affect spatial anchoring in ViTs?

Our hypothesis is simple: ViT representations live in a model’s internal positional reference frame. Therefore, for multi-view tasks, scene-level geometric structure may naturally emerge when this internal frame is consistently aligned across views. We propose a simple, training-free token re-indexing operation.



Figure 2. Illustration of token re-indexing. The upper and bottom represent two feature maps that contain overlapping regions (in pixel space, annotated in red color) along the horizontal axis.

Setup. We adopt the same content-position isolation settings as per Section 4.1. With two overlapping crops I_1 and I_2 , we introduce a training-free token re-indexing procedure that enforces PE kernel alignment across views, as illustrated in Figure 2. Simply, we ensure that tokens that correspond to the same scene-space location within the overlaps are assigned with identical positional indices. The details of the token re-indexing for different positional encoding methods are presented in the supplementary.

Results. Table 4 reports token-wise cosine similarities before and after re-indexing across all positional encoding types. With aligned PEs, token similarities are consistently restored across all models, without any training. This “free-

Table 4. Token re-indexing performance. Aligned PE kernels increase similarity, indicating improved spatial consistency.

	Vanilla PE			Aligned PE			
	PE	$\Delta x = 1$	$\Delta x = 2$	$\Delta x = 3$	$\Delta x = 1$	$\Delta x = 2$	$\Delta x = 3$
DINO	Abs.	0.9782	0.9765	0.9627	0.9980	0.9809	0.9766
DINOv2	Abs.	0.6775	0.5760	0.5272	0.7446	0.6318	0.5782
DINOv3	Rot.	0.9261	0.7377	0.6564	0.9744	0.9657	0.9616
MLCD	Rot.	0.8209	0.7345	0.6786	0.8412	0.7660	0.7175
I-JEPA	Abs.	0.7318	0.7283	0.7280	0.8646	0.8576	0.8568
DeiT	Abs.	0.8184	0.8003	0.7947	0.9400	0.9107	0.9031
SigLIP2	Abs.	0.6468	0.6920	0.6872	0.7143	0.6312	0.6199
BEiT	Rel.	0.9998	0.9997	0.9997	0.9999	0.9999	0.9999
Data2Vec	Rel.	0.9850	0.9678	0.9469	0.9978	0.9948	0.9997
ViT	Abs.	0.7913	0.7737	0.7416	0.9498	0.9354	0.9338
CLIP	Abs.	0.6758	0.6665	0.6711	0.9234	0.8844	0.8652
SAM	Abs.	0.9969	0.9945	0.9921	0.9977	0.9971	0.9971
Swin	Rel.	0.6928	0.6928	0.5899	0.8448	0.8293	0.8189

lunch” improvement provides direct evidence that the observed degradation arises from model’s view-dependent internal positional reference frames, rather than intrinsic differences in architectural modeling.

Token re-indexing is not proposed as a practical algorithm, but as a controlled intervention to test whether positional alignment alone is sufficient to restore spatial anchoring. The success of this training-free alignment indicates that geometric information is preserved in the representation but expressed relative to mismatched PEs in multi-view tasks.

5.2. Implicit Positional Alignment in VGGT

With the role of PE kernel misalignment clarified, it remains an open question that:

Why do some multi-view systems succeed despite being built on ViT backbones with standard positional embeddings?

VGGT provides a particularly instructive case. It employs a ViT backbone to extract per-view token features, followed by an aggregator that jointly processes tokens across views. Importantly, the positional encoding mechanism of its ViT backbone (DINOv2) is left unchanged. In this section, we analyze the behavior of VGGT for multi-view geometry under the lens of PE kernels.

Setup. To understand how VGGT achieves robust multi-view representation, we analyze the layer-wise evolution of cross-view token similarity within its aggregator. We use the same overlapping-crop dataset construction as in Section 4.1, which induces positional reference mismatch while preserving identical visual content.

First, for corresponding tokens across views, we measure cosine similarity as a function of aggregator depth (24-layer in total). We repeat this analysis for increasing horizontal displacements $\Delta x \in \{1, 2, 3\}$. Second, for each aggregation layer, we train lightweight MLP to predict the row and column indices from individual token features under $\Delta x = 3$, for probing how much positional information are preserved for each layer. These experiments provide a controlled way to probe the evolution of positional information and spatial consistency across aggregation layers.

Results. As shown in Figure 3, across all displacement magnitudes, similarity initially decreases in the early layers, reaching a minimum around layers 6–10. This effect is more pronounced for larger Δx , where positional reference mismatch is stronger. Beyond the mid-depth layers, similarity begins to recover and increases rapidly in the later stages of the aggregator. By the final layers, similarity converges toward near-perfect alignment for all Δx values.

Similarly, the positional decoding probes present a complementary behavior. The position indices remain highly

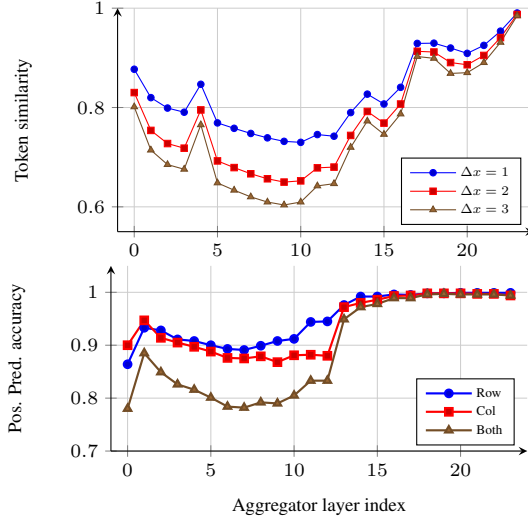


Figure 3. Layer-wise evaluation for the aggregator of VGGT. **Upper:** cross-view token similarity. We report cosine similarity between corresponding tokens across views as a function of the VGGT aggregator depth (24 layers), for increasing horizontal displacements $\Delta x = \{1, 2, 3\}$. As depth increases, similarity consistently recovers and converges toward near-perfect ($\text{Sim} \approx 1$) alignment for all displacements. **Lower:** position decodability. we report probing accuracy for predicting the positional index (row, column, both) for each token under $\Delta x = 3$.

decodable throughout the aggregator, while the positional signals surge significantly at the 13th layer, reaching almost 100% decoding accuracy afterwards.

VGGT does not remove positional information from tokens, nor modify the backbone PE scheme. These results show that VGGT may learn a robust multi-view representation by implicitly inferring a canonical latent coordinate system that reconciles PEs across views.

6. Discussion

This work identifies a previously unarticulated failure mode in ViTs, in which spatial anchoring degrades under PE mismatch. Unlike prior analyses (El Banani et al., 2024; Chen et al., 2025) that examine ViT representations as inseparable tokens, our study isolates how much of a model’s spatial behavior originates from visual content versus the positional mechanism itself.

Under Unified Lens of Positional Embeddings. Several prior works (Sun et al., 2021; Li et al., 2021b) have reported that PEs can degrade geometric alignment, correspondence accuracy, or cross-view consistency in ViTs. By holding visual content fixed and selectively intervening on PEs, our experiments isolate the causal role of PEs in shaping geometric representations, resulting in a more nuanced and unified interpretation.

Under which these previously reported failure cases can be understood as consequences of misaligned PE-induced

spatial kernels, rather than as evidence that PEs themselves are harmful. When PEs are defined with respect to image-space coordinate systems, tokens extracted from different views or crops may be embedded in incompatible positional reference frames, even when they correspond to identical scene content. As stated in Section 5.1, a simple training-free re-indexing can significantly recover a large fraction of the lost geometric correspondence. The success of VGGT provides further confirms this insight.

Overall, our analysis provides a unified view of prior PE failures, that multi-view geometric degradation arises not from the presence of PEs or a lack of geometric information, but from the inconsistent PEs across views.

Design Implications. Our analysis does not propose a new positional encoding scheme. Instead, it suggests that architectural gains may arise from how positional information is represented, aligned, or transformed, rather than always focusing on strengthening visual feature extraction. In particular, our experimental results demonstrate that a significant portion of geometric inconsistency originates from inconsistent PEs. This suggests that architectural improvements should prioritize PE consistency for multi-view tasks.

Limitations and Future Work. Our analysis isolates the representational role of PEs at inference time. This probing setup reveals how PEs structure spatial relations in pre-trained ViTs, but it does not capture how a model would behave if positional mechanisms were changed during training. Thus, our conclusions speak to the inherent dependencies learned under standard PE schemes rather than reflecting how a model would adapt if retrained under altered positional encoding schemes entirely. Inspired by recent works such as (Li et al., 2025; Gopalakrishnan et al., 2025), an interesting next step is to move beyond purely image-space positional frames. Our token re-indexing and VGGT probing experiment suggest that part of the failures of multi-view representation learning arises from PE misalignment rather than representation collapse. This points toward future positional designs that incorporate geometric constraints, such as multi-view alignment or scene-aware PE systems, to better bridge image-space indexing with scene-space structure.

7. Conclusion

We presented a set of controlled experiments examining how positional embeddings (PEs) influence several spatial properties of vision transformer (ViT) representations. Across 14 foundation ViTs, we showed that PEs critically regulate spatial interactions and geometric consistency for multi-view representations. We hope these findings provide a clearer empirical basis for future work on understanding and designing positional mechanisms in ViTs and multi-view geometry.

Impact Statement

This work provides a fundamental analysis of how positional embeddings shape spatial reasoning in vision transformers, particularly in multi-view settings. By isolating positional mechanisms from visual content, our findings clarify why existing models may succeed or fail under viewpoint changes, and provide diagnostic tools for analyzing spatial consistency at the representation level.

Overall, we view this work as contributing foundational insights into representation learning, with the primary impact that provides a basis for more principled analysis and design of positional mechanisms for future vision models.

References

- Amir, S., Gandelsman, Y., Bagon, S., and Dekel, T. Deep vit features as dense visual descriptors. *arXiv preprint arXiv:2112.05814*, 2(3):4, 2021.
- An, X., Yang, K., Dai, X., Feng, Z., and Deng, J. Multi-label cluster discrimination for visual representation learning. In *ECCV*, 2024.
- Assran, M., Duval, Q., Misra, I., Bojanowski, P., Vincent, P., Rabbat, M., LeCun, Y., and Ballas, N. Self-supervised learning from images with a joint-embedding predictive architecture. In *Proceedings of the IEEE/CVF Conference on Computer Vision and Pattern Recognition*, pp. 15619–15629, 2023.
- Baevski, A., Hsu, W.-N., Xu, Q., Babu, A., Gu, J., and Auli, M. Data2vec: A general framework for self-supervised learning in speech, vision and language. In *International conference on machine learning*, pp. 1298–1312. PMLR, 2022.
- Bai, Y., Li, H., and Huang, Q. Positional encoding field. *arXiv preprint arXiv:2510.20385*, 2025.
- Bao, H., Dong, L., Piao, S., and Wei, F. Beit: BERT pre-training of image transformers. In *The Tenth International Conference on Learning Representations, ICLR 2022, Virtual Event, April 25-29, 2022*. OpenReview.net, 2022. URL <https://openreview.net/forum?id=p-BhZSz59o4>.
- Carion, N., Massa, F., Synnaeve, G., Usunier, N., Kirillov, A., and Zagoruyko, S. End-to-end object detection with transformers. In *European conference on computer vision*, pp. 213–229. Springer, 2020.
- Chang, J.-R. and Chen, Y.-S. Pyramid stereo matching network. In *Proceedings of the IEEE conference on computer vision and pattern recognition*, pp. 5410–5418, 2018.
- Chen, C., Panda, R., and Fan, Q. Regionvit: Regional-to-local attention for vision transformers. In *The Tenth International Conference on Learning Representations, ICLR 2022, Virtual Event, April 25-29, 2022*. OpenReview.net, 2022. URL https://openreview.net/forum?id=T_V3uLix7V.
- Chen, M., Zhang, L., Feng, R., Xue, X., and Feng, J. Rethinking local and global feature representation for dense prediction. *Pattern Recognition*, 135:109168, 2023.
- Chen, Y., Chen, X., Chen, A., Pons-Moll, G., and Xiu, Y. Feat2gs: Probing visual foundation models with gaussian splatting. In *Proceedings of the Computer Vision and Pattern Recognition Conference*, pp. 6348–6361, 2025.
- Chu, X., Tian, Z., Zhang, B., Wang, X., and Shen, C. Conditional positional encodings for vision transformers. In *The Eleventh International Conference on Learning Representations, ICLR 2023, Kigali, Rwanda, May 1-5, 2023*. OpenReview.net, 2023. URL <https://openreview.net/forum?id=3KWnuT-R1bh>.
- Dosovitskiy, A., Fischer, P., Ilg, E., Hausser, P., Hazirbas, C., Golkov, V., Van Der Smagt, P., Cremers, D., and Brox, T. Flownet: Learning optical flow with convolutional networks. In *Proceedings of the IEEE international conference on computer vision*, pp. 2758–2766, 2015.
- Dosovitskiy, A., Beyer, L., Kolesnikov, A., Weissenborn, D., Zhai, X., Unterthiner, T., Dehghani, M., Minderer, M., Heigold, G., Gelly, S., Uszkoreit, J., and Houlsby, N. An image is worth 16x16 words: Transformers for image recognition at scale. In *9th International Conference on Learning Representations, ICLR 2021, Virtual Event, Austria, May 3-7, 2021*. OpenReview.net, 2021. URL <https://openreview.net/forum?id=YicbFdNTTy>.
- El Banani, M., Raj, A., Maninis, K.-K., Kar, A., Li, Y., Rubinstein, M., Sun, D., Guibas, L., Johnson, J., and Jampani, V. Probing the 3d awareness of visual foundation models. In *Proceedings of the IEEE/CVF Conference on Computer Vision and Pattern Recognition*, pp. 21795–21806, 2024.
- Gopalakrishnan, A., Csordás, R., Schmidhuber, J., and Mozer, M. C. Decoupling the “what” and “where” with polar coordinate positional embeddings. *arXiv preprint arXiv:2509.10534*, 2025.
- He, K., Chen, X., Xie, S., Li, Y., Dollár, P., and Girshick, R. Masked autoencoders are scalable vision learners. In *Proceedings of the IEEE/CVF conference on computer vision and pattern recognition*, pp. 16000–16009, 2022.

- He, P., Liu, X., Gao, J., and Chen, W. Deberta: decoding-enhanced bert with disentangled attention. In *9th International Conference on Learning Representations, ICLR 2021, Virtual Event, Austria, May 3-7, 2021*. OpenReview.net, 2021. URL <https://openreview.net/forum?id=XPZIaotutsD>.
- Howard, J. Imagenette: A smaller subset of 10 easily classified classes from imagenet, March 2019. URL <https://github.com/fastai/imagenette>.
- Im, S., Jeon, H., Lin, S., and Kweon, I. S. Dpsnet: End-to-end deep plane sweep stereo. In *7th International Conference on Learning Representations, ICLR 2019, New Orleans, LA, USA, May 6-9, 2019*. OpenReview.net, 2019. URL <https://openreview.net/forum?id=ryeYHi0ctQ>.
- Kendall, A., Martirosyan, H., Dasgupta, S., and Henry, P. End-to-end learning of geometry and context for deep stereo regression. In *IEEE International Conference on Computer Vision, ICCV 2017, Venice, Italy, October 22-29, 2017*, pp. 66–75. IEEE Computer Society, 2017. doi: 10.1109/ICCV.2017.17. URL <https://doi.org/10.1109/ICCV.2017.17>.
- Kirillov, A., Mintun, E., Ravi, N., Mao, H., Rolland, C., Gustafson, L., Xiao, T., Whitehead, S., Berg, A. C., Lo, W.-Y., et al. Segment anything. In *Proceedings of the IEEE/CVF international conference on computer vision*, pp. 4015–4026, 2023.
- Li, R., Yi, B., Liu, J., Gao, H., Ma, Y., and Kanazawa, A. Cameras as relative positional encoding. *arXiv preprint arXiv:2507.10496*, 2025.
- Li, Y., Zhang, K., Cao, J., Timofte, R., and Gool, L. V. Localvit: Bringing locality to vision transformers. *CoRR*, abs/2104.05707, 2021a. URL <https://arxiv.org/abs/2104.05707>.
- Li, Z., Liu, X., Drenkow, N., Ding, A. S., Creighton, F. X., Taylor, R. H., and Unberath, M. Revisiting stereo depth estimation from a sequence-to-sequence perspective with transformers. In *2021 IEEE/CVF International Conference on Computer Vision, ICCV 2021, Montreal, QC, Canada, October 10-17, 2021*, pp. 6177–6186. IEEE, 2021b. doi: 10.1109/ICCV48922.2021.00614. URL <https://doi.org/10.1109/ICCV48922.2021.00614>.
- Liu, T., Ye, X., Zhao, W., Pan, Z., Shi, M., and Cao, Z. When epipolar constraint meets non-local operators in multi-view stereo. In *Proceedings of the IEEE/CVF international conference on computer vision*, pp. 18088–18097, 2023.
- Liu, Y., Wang, T., Zhang, X., and Sun, J. Petr: Position embedding transformation for multi-view 3d object detection. In *European conference on computer vision*, pp. 531–548. Springer, 2022.
- Liu, Z., Hu, H., Lin, Y., Yao, Z., Xie, Z., Wei, Y., Ning, J., Cao, Y., Zhang, Z., Dong, L., Wei, F., and Guo, B. Swin transformer V2: scaling up capacity and resolution. *CoRR*, abs/2111.09883, 2021a. URL <https://arxiv.org/abs/2111.09883>.
- Liu, Z., Lin, Y., Cao, Y., Hu, H., Wei, Y., Zhang, Z., Lin, S., and Guo, B. Swin transformer: Hierarchical vision transformer using shifted windows. *CoRR*, abs/2103.14030, 2021b. URL <https://arxiv.org/abs/2103.14030>.
- Mehl, L., Schmalfuss, J., Jahedi, A., Nalivayko, Y., and Bruhn, A. Spring: A high-resolution high-detail dataset and benchmark for scene flow, optical flow and stereo. In *Proceedings of the IEEE/CVF Conference on Computer Vision and Pattern Recognition*, pp. 4981–4991, 2023.
- Oquab, M., Darce, T., Moutakanni, T., Vo, H. V., Szafraniec, M., Khalidov, V., Fernandez, P., Haziza, D., Massa, F., El-Nouby, A., Assran, M., Ballas, N., Galuba, W., Howes, R., Huang, P., Li, S., Misra, I., Rabat, M., Sharma, V., Synnaeve, G., Xu, H., Jégou, H., Mairal, J., Labatut, P., Joulin, A., and Bojanowski, P. Dinnov2: Learning robust visual features without supervision. *Trans. Mach. Learn. Res.*, 2024, 2024. URL <https://openreview.net/forum?id=a68SUT6zFt>.
- Park, N. and Kim, S. How do vision transformers work? In *The Tenth International Conference on Learning Representations, ICLR 2022, Virtual Event, April 25-29, 2022*. OpenReview.net, 2022. URL <https://openreview.net/forum?id=D78Go4hVcx0>.
- Press, O., Smith, N. A., and Lewis, M. Train short, test long: Attention with linear biases enables input length extrapolation. In *The Tenth International Conference on Learning Representations, ICLR 2022, Virtual Event, April 25-29, 2022*. OpenReview.net, 2022. URL <https://openreview.net/forum?id=R8sQPpGCv0>.
- Radford, A., Kim, J. W., Hallacy, C., Ramesh, A., Goh, G., Agarwal, S., Sastry, G., Askell, A., Mishkin, P., Clark, J., et al. Learning transferable visual models from natural language supervision. In *International conference on machine learning*, pp. 8748–8763. PMLR, 2021.
- Raghu, M., Unterthiner, T., Kornblith, S., Zhang, C., and Dosovitskiy, A. Do vision transformers see like convolutional neural networks? *Advances in neural information processing systems*, 34:12116–12128, 2021.

- Shaw, P., Uszkoreit, J., and Vaswani, A. Self-attention with relative position representations. *arXiv preprint arXiv:1803.02155*, 2018.
- Siméoni, O., Vo, H. V., Seitzer, M., Baldassarre, F., Oquab, M., Jose, C., Khalidov, V., Szafraniec, M., Yi, S., Ramamonjisoa, M., et al. Dinov3. *arXiv preprint arXiv:2508.10104*, 2025.
- Su, J., Ahmed, M. H. M., Lu, Y., Pan, S., Bo, W., and Liu, Y. Roformer: Enhanced transformer with rotary position embedding. *Neurocomputing*, 568:127063, 2024. doi: 10.1016/J.NEUCOM.2023.127063. URL <https://doi.org/10.1016/j.neucom.2023.127063>.
- Sun, D., Yang, X., Liu, M.-Y., and Kautz, J. Pwc-net: Cnns for optical flow using pyramid, warping, and cost volume. In *Proceedings of the IEEE conference on computer vision and pattern recognition*, pp. 8934–8943, 2018.
- Sun, J., Shen, Z., Wang, Y., Bao, H., and Zhou, X. Loftr: Detector-free local feature matching with transformers. In *Proceedings of the IEEE/CVF conference on computer vision and pattern recognition*, pp. 8922–8931, 2021.
- Teed, Z. and Deng, J. Raft: Recurrent all-pairs field transforms for optical flow. In *European conference on computer vision*, pp. 402–419. Springer, 2020.
- Touvron, H., Cord, M., Douze, M., Massa, F., Sablayrolles, A., and Jegou, H. Training data-efficient image transformers & distillation through attention. In *International Conference on Machine Learning*, volume 139, pp. 10347–10357, July 2021.
- Tschannen, M., Gritsenko, A., Wang, X., Naeem, M. F., Alabdulmohsin, I., Parthasarathy, N., Evans, T., Beyer, L., Xia, Y., Mustafa, B., et al. Siglip 2: Multilingual vision-language encoders with improved semantic understanding, localization, and dense features. *arXiv preprint arXiv:2502.14786*, 2025.
- Tu, Z., Talebi, H., Zhang, H., Yang, F., Milanfar, P., Bovik, A., and Li, Y. Maxvit: Multi-axis vision transformer. In *European conference on computer vision*, pp. 459–479. Springer, 2022.
- Vaswani, A., Shazeer, N., Parmar, N., Uszkoreit, J., Jones, L., Gomez, A. N., Kaiser, Ł., and Polosukhin, I. Attention is all you need. *Advances in neural information processing systems*, 30, 2017.
- Wang, J., Chen, M., Karaev, N., Vedaldi, A., Rupprecht, C., and Novotny, D. Vggt: Visual geometry grounded transformer. In *Proceedings of the Computer Vision and Pattern Recognition Conference*, pp. 5294–5306, 2025a.
- Wang, Y., Zhou, J., Zhu, H., Chang, W., Zhou, Y., Li, Z., Chen, J., Pang, J., Shen, C., and He, T. π^3 : Scalable permutation-equivariant visual geometry learning, 2025b. URL <https://arxiv.org/abs/2507.13347>.
- Wimmer, T., Truong, P., Rakotosaona, M.-J., Oechsle, M., Tombari, F., Schiele, B., and Lenssen, J. E. Anyup: Universal feature upsampling. *arXiv preprint arXiv:2510.12764*, 2025.
- Wu, K., Peng, H., Chen, M., Fu, J., and Chao, H. Rethinking and improving relative position encoding for vision transformer. In *Proceedings of the IEEE/CVF international conference on computer vision*, pp. 10033–10041, 2021.
- Yang, L., Kang, B., Huang, Z., Xu, X., Feng, J., and Zhao, H. Depth anything: Unleashing the power of large-scale unlabeled data. In *Proceedings of the IEEE/CVF conference on computer vision and pattern recognition*, pp. 10371–10381, 2024.
- Yuan, Y., Fu, R., Huang, L., Lin, W., Zhang, C., Chen, X., and Wang, J. Hrformer: High-resolution transformer for dense prediction. *arXiv preprint arXiv:2110.09408*, 2021.
- Zhang, H., Li, F., Liu, S., Zhang, L., Su, H., Zhu, J., Ni, L. M., and Shum, H. DINO: DETR with improved denoising anchor boxes for end-to-end object detection. In *The Eleventh International Conference on Learning Representations, ICLR 2023, Kigali, Rwanda, May 1-5, 2023*. OpenReview.net, 2023a. URL <https://openreview.net/forum?id=3mRwyG5one>.
- Zhang, Z., Peng, R., Hu, Y., and Wang, R. Geomvsnet: Learning multi-view stereo with geometry perception. In *Proceedings of the IEEE/CVF Conference on Computer Vision and Pattern Recognition*, pp. 21508–21518, 2023b.

A. Technical Details

This section presents technical details regarding how we perform positional weighting, the derivation of relative and rotary positional kernels, and how do we construct the 4D correlation volume and relevant metrics to capture epipolar peak response.

A.1. Positional Weighting

We define a scalar coefficient $\omega \in [0, 1]$, referred to as the *positional weight*, that modulates the strength of the positional signal. We adapt the formulation to each type of positional encoding used in modern ViTs.

A.1.1. ABSOLUTE AND RELATIVE PEs

Absolute PEs (ViT, DeiT, CLIP). Absolute PEs are directly scaled by the weighting factor:

$$\mathbf{P}' = \omega \cdot \mathbf{P}, \quad (11)$$

where \mathbf{P} denotes the pretrained absolute PE matrix.

Relative PEs (Swin, SwinV2, BEiT, Data2Vec). Similar to absolute PEs, for models employing relative position bias or continuous positional MLPs, we apply a multiplicative scaling:

$$\mathbf{B}' = \omega \cdot \mathbf{B}, \quad (12)$$

where \mathbf{B} represents either the discrete bias table or the learned continuous bias embedding.

A.1.2. ROTARY PEs

RoPE define a rotation operator $\mathbf{R}_\theta = \begin{pmatrix} \cos \theta & -\sin \theta \\ \sin \theta & \cos \theta \end{pmatrix}$.

Crucially, RoPE is multiplicative in the sense of a rotation; there is no additive positional vector to “scale” as in absolute and relative PEs. Therefore, weighting the positional effect must operate on the rotation itself, not by multiplying with a scalar.

Differently, RoPE encode positions by *rotating* each 2D subspace of the query/key vectors by a phase that depends on the token index p and the subspace frequency ω_i . For a 2D slice (x_{2i}, x_{2i+1}) of a vector $x \in \mathbb{R}^d$ (with d even), the standard RoPE transform is $R(\theta_i) \begin{bmatrix} x_{2i} \\ x_{2i+1} \end{bmatrix}$, where $\theta_i = p\omega_i$ and $\omega_i = 10000^{-2i/d}$. The conceptually clean approach is to scale the phase:

$$R_w(\theta_i) := R(w\theta_i) = \begin{bmatrix} \cos(w\theta_i) & -\sin(w\theta_i) \\ \sin(w\theta_i) & \cos(w\theta_i) \end{bmatrix}. \quad (13)$$

Such that $R_0(\theta_i) = I$ and $R_1(\theta_i) = R(\theta_i)$. For fixed p , decreasing w reduces the angular rate across positions, thereby softening position sensitivity without altering vector norms.

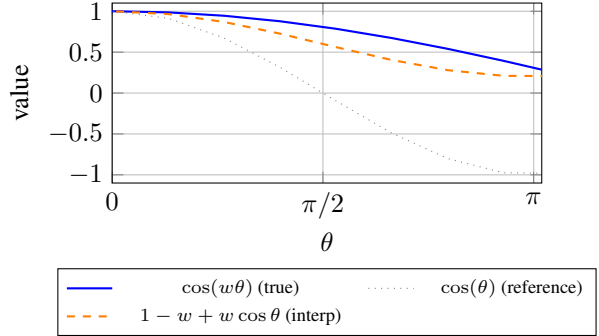


Figure 4. Comparison of phase-scaling vs interpolation for RoPE. The interpolated rotation $(1-w)I + wR(\theta)$ closely follows the true phase-scaled rotation $R(w\theta)$ in magnitude, validating it as an effective implementation surrogate.

Therefore, the attention kernel induced by RoPE (through $q^\top k$ after rotation) varies smoothly with w , preserving relative geometry while controlling positional contrast.

However, direct updating θ is not supported in many libraries. Thus, to ease the implementation, we interpolate between the identity (no rotation) and full rotation as:

$$\cos' = 1 - \omega + \omega \cos \theta, \quad \sin' = \omega \sin \theta. \quad (14)$$

This formulation preserves orthogonality while continuously modulating the angular contribution of positional rotation.

However, as many libraries cache only $(\cos \theta, \sin \theta)$, not θ itself, we use an effective surrogate is to interpolate the rotation toward the identity:

$$\tilde{R}_w \approx (1 - w)I + wR(\theta), \quad (15)$$

such that:

$$\begin{cases} \cos'(p, i) = (1 - w) \cdot 1 + w \cdot \cos \theta_i = 1 - w + w \cos \theta_i, \\ \sin'(p, i) = (1 - w) \cdot 0 + w \cdot \sin \theta_i = w \sin \theta_i. \end{cases} \quad (16)$$

While (15) is not equal to $R(w\theta)$ for intermediate w , it is a stable and faithful blend between identity and the full rotation.

A.2. Epipolar Peak Response Capturing

A.2.1. 4D CORRELATION VOLUME

To measure how well a model preserves epipolar geometry, we construct a full *4D correlation volume* between the left and right feature maps. This formulation is conceptually related to correlation layers in optical flow (Dosovitskiy et al., 2015; Sun et al., 2018; Teed & Deng, 2020) that retains the entire 2D search space.

Given normalized feature embeddings $\hat{\mathbf{F}}_L, \hat{\mathbf{F}}_R \in \mathbb{R}^{B \times C \times H \times W}$, the 4D correlation is defined as:

$$\mathbf{C}(x, y, x', y') = \hat{\mathbf{F}}_L(x, y)^\top \hat{\mathbf{F}}_R(x', y'), \quad (17)$$

yielding a dense affinity tensor $\mathbf{C} \in \mathbb{R}^{B \times H \times W \times H \times W}$. This volume encodes all potential cross-view correspondences without imposing rectification or epipolar-line constraints.

To obtain a differentiable point estimate of correspondence, we apply a spatial softmax over the search domain:

$$p(x', y' | x, y) = \frac{\exp(\tau \mathbf{C}(x, y, x', y'))}{\sum_{x'', y''} \exp(\tau \mathbf{C}(x, y, x'', y''))}, \quad (18)$$

where τ controls the sharpness. The expected displacement is then:

$$\hat{\mathbf{u}}(x, y) = \mathbb{E}_{p(x', y' | x, y)}[(x' - x, y' - y)]. \quad (19)$$

This “soft argmax” provides a differentiable approximation to hard matching and is widely used in deep stereo and multi-view reconstruction (Im et al., 2019; Li et al., 2021b; Zhang et al., 2023b; Liu et al., 2023).

Rectified Stereo as a Special Case. Similar to the traditional stereo cost volumes (Kendall et al., 2017; Chang & Chen, 2018), rectified stereo geometry restricts the *true* matches to lie on the horizontal epipolar line $y' = y$. Under this geometric constraint, the relevant slice of the 4D volume reduces to a standard 1D cost volume:

$$C(x, y, d) = \mathbf{C}(x, y, x + d, y), \quad (20)$$

where d is the horizontal displacement. The disparity estimate is then obtained through the familiar soft-argmin operation:

$$\hat{d}(x, y) = \sum_d d \cdot \text{softmax}(\tau C(x, y, d)). \quad (21)$$

Thus, the traditional 1D stereo formulation emerges naturally as the *rectified geometric slice* of the full 4D correspondence volume, rather than a separate construction.

A.2.2. METRICS

We evaluate how faithfully the feature-induced cost volume reflects the true epipolar geometry.

End-Point Error (EPE). EPE measures the average absolute deviation between the predicted and ground-truth disparities:

$$\text{EPE} = \frac{1}{|\Omega|} \sum_{(x, y) \in \Omega} |\hat{d}(x, y) - d^{gt}(x, y)|. \quad (22)$$

Lower values indicate that the peak of the similarity distribution aligns closely with the correct epipolar correspondence.

Epipolar Recall@n. To quantify how sharply the correlation volume peaks around the correct match, we compute Recall@n. The percentage of pixels for which ground truth disparity lies among the top- n highest responses in $C(x, y, d)$. A higher Recall@n indicates a more confident and better localized epipolar peak.

B. More Experiments

B.1. PE Strength Sweep

Unlike convolutional networks, which enforce spatial continuity through local receptive fields, ViTs operate on sets of tokens with no inherent notion of spatial adjacency. In principle, attention is permutation-invariant, meaning that any token could interact with any other, independent of their image positions. Yet, in practice, ViT features exhibit surprisingly smooth spatial organization where neighboring patches often encode correlated information and preserve local geometry. This raises a fundamental, unanswered question:

Where does this spatial continuity come from in a model with no built-in notion of space?

B.1.1. METHOD

As discussed in Section 3.2, we hypothesize that PEs are responsible for inducing an *implicit spatial kernel* that governs how attention strength decays with distance. To test this, we design a token-offset probing experiment that directly measures how token similarity varies with spatial displacement and the weight of PEs. If PEs truly modulate inter-token interactions, reducing their weight should weaken similarity, while a coherent spatial representation should exhibit decreasing similarity with increasing distance. By observing the shape and steepness of this decay, we can then understand how positional signals translate into spatial inductive bias.

B.1.2. SETUP

Given a reference token $\mathcal{T}_{i,j}$ at spatial position (i, j) , we examine its relationship with a displaced token $\mathcal{T}_{i+\Delta x, j+\Delta y}$ located at an offset $(\Delta x, \Delta y)$ within the same feature map, as illustrated in Figure 5. We evaluate the *cosine similarity* between tokens $\mathcal{T}_{i,j}$ and $\mathcal{T}_{i+\Delta x, j+\Delta y}$ to understand

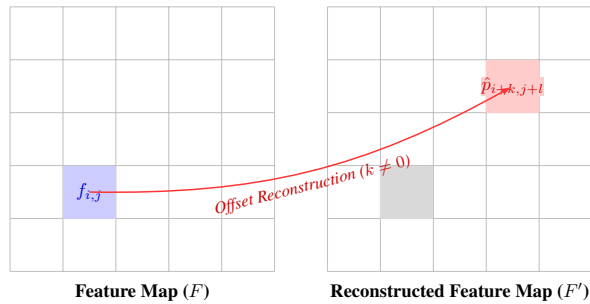


Figure 5. Visualization of token-offset probing. A source token $f_{i,j}$ from F (left) is used to reconstruct $\hat{p}_{i+k, j+l}$ at an offset position in F' (right), with the original (i, j) location grayed out. Note that flattened transformer tokens lack 2D spatial relations. We reshape them into a feature map layout for interpretability.

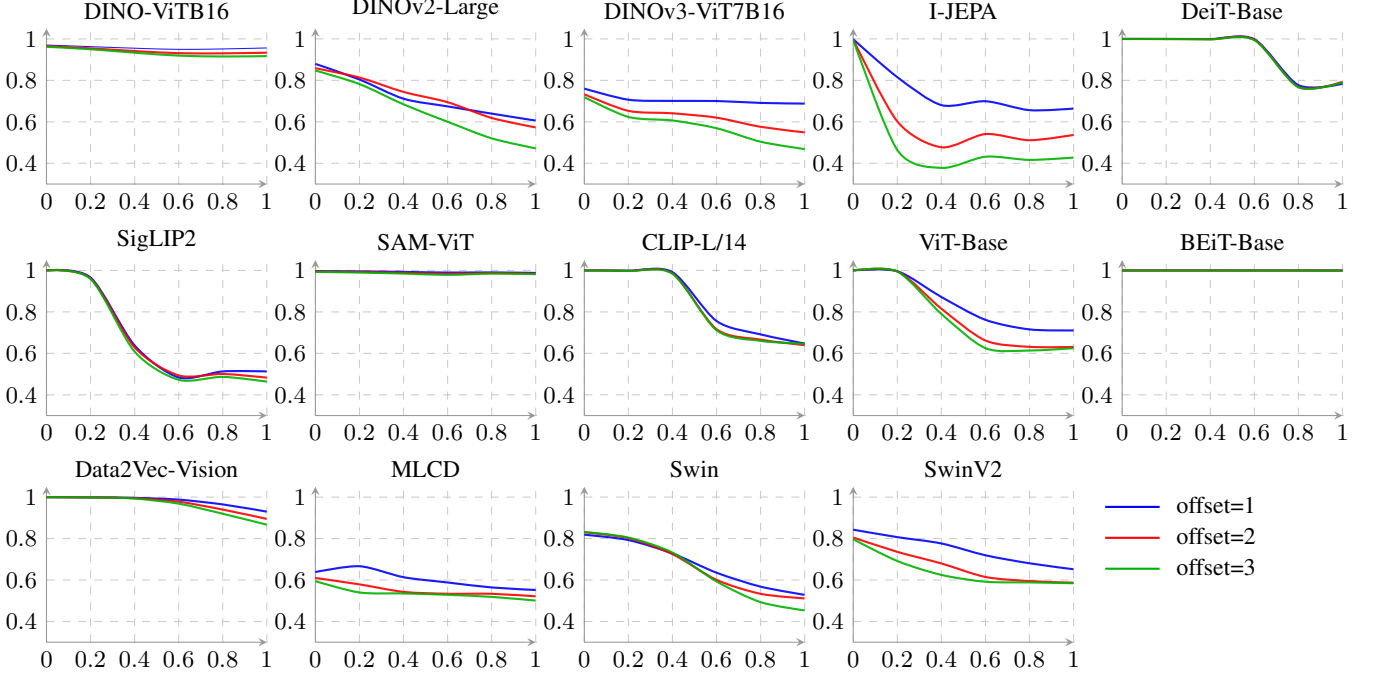


Figure 6. Impact of positional weighting on spatial similarity across models. Each subplot shows how token similarity varies with PE strength ω at different spatial offsets.

the local geometric continuity. We report the average similarity over all valid displacement pairs. For simplicity, we consider symmetric integer offsets $k \in \{1, 2, 3\}$ with $\Delta x = \Delta y = k$, and apply a decaying PE strength $\omega \in \{0.0, 0.2, 0.4, 0.6, 0.8, 1.0\}$.

We carry out our experiments based on *Imagenette* (Howard, 2019) with a size of 224×224 . Most transformer-based foundation vision encoders use a patch size of 16 or 14, resulting in a fixed grid of 14×14 or 16×16 . The feature grids are downsampled to 16×16 for the models that require a larger input size.

B.1.3. ANALYSES

Figure 6 illustrates the token-offset experiment results across 14 visual foundation models.

Positional embeddings go beyond providing coordinates. Apart from BEiT, larger offsets consistently weaken the similarity, reflecting a notion of local continuity. This behavior indicates that positional components contribute explicitly to spatial discrimination, which aligns with Section 3.2. With decayed PE strength, the model shifts from a locally structured representation to a globally homogeneous one. Interestingly, we observe no significant differences among various PE strength and token offset settings for BEiT, indicating the lack of locality. This observation also aligns with our later experiment in Section 4.2. Additionally, averaged over all encoders, the area under the curve (AUC) drops by $\sim 8\%$ from lowest to highest PE strength, while the end-to-

end decay (PE strength from 0 to 1) rises by $\sim 58\%$. In this protocol, PE directly controls how concentrated (local) the token interactions are.

B.2. Do tokens know where they are?

To understand if tokens are aware of its position as expected, we design a simple probing experiment to evaluate the positional awareness of various ViT-based foundation models. Given an encoder’s feature map $\mathbf{F} \in \mathbb{R}^{C \times H \times W}$ extracted from an input image, we train a lightweight *position predictor* that takes either a single feature token or a local $N \times N$ neighborhood and predicts its absolute row and column indices (r, c) on the feature grid. Both row and column positions are modeled as categorical classification tasks with cross-entropy losses. The encoder is frozen during training, and only the probe is optimized. The evaluation metrics include separate accuracies for row and column predictions, as well as the joint “both” accuracy for exact 2D localization.

Table 5 demonstrates that nearly all tested ViTs exhibit strong positional awareness, even though their encoding mechanisms differ widely. Models trained with explicit absolute or relative embeddings (e.g., DINO, DEiT, SAM) achieve almost perfect localization accuracy. In general, all position encoding methods allow positional information to be linearly recovered, suggesting that positional cues are deeply embedded in the learned representation regardless of the encoding formulation.

Differently, Swin/SwinV2 rely on local windows and shifted

	row	col	both
DINO	0.999	0.999	0.999
DINOv2	0.926	0.961	0.893
DINOv3	0.796	0.846	0.687
I-JEPA	0.995	0.998	0.994
DEiT	0.996	0.996	0.993
Siglip2	0.995	0.993	0.989
BeiT	0.822	0.813	0.658
dat2vec	0.994	0.988	0.982
MLCD	0.848	0.801	0.697
ViT	0.997	0.997	0.994
SAM	0.979	0.973	0.956
CLIP	0.888	0.874	0.810
Swin	0.803	0.682	0.561
SwinV2	0.602	0.418	0.270

Table 5. Token position prediction accuracy. Values denote the probability of correctly predicting the token’s absolute row, column, and joint 2D index.

windows. Token locations in Swin models are explicitly encoded directly, we might expect it to rely less on positional embeddings. By design, Swin series models emphasize relative positions within windows and hierarchical structure, so that absolute 2D positions are much less linearly decodable in those models. In addition, rotary embedding methods such as DINOv3 and MLCD exhibit also a slight weaker performance than those absolute and relative embedding method. We believe it is because rotary encoding preserves direction (angular displacement) without encoding scales, thus it does not give the model a unique positional signature tied to a specific grid location. As a result, recovering exact row/column indices becomes harder.

B.3. Do Tokens Preserve Spatial Identity?

Local continuity alone does not reveal whether the model preserves spatial identity. Thus, we further investigate:

Without PEs, are tokens at different positions distinguishable in feature space?

Following the setup in Section B.1, we further measure whether a displaced token $\mathcal{T}i + \Delta x, j + \Delta y$ can be linearly reconstructed from its reference $\mathcal{T}i, j$ using a single linear layer.

Results. As shown in Table 6, when PEs are removed, reconstruction similarity remains uniformly high across all offsets, indicating that features at different spatial locations become nearly interchangeable. This suggests that without positional cues, ViTs drift toward a globally invariant representation space, effectively removing positional identity. In contrast, with PEs enabled, reconstruction similarity decreases with increasing offset for almost all models. This indicates that tokens encode spatially localized information that cannot be linearly inferred from neighboring positions. PEs therefore preserve spatial distinctiveness, not just local continuity.

Notably, models such as DINO1/2, MLCD, and Swin1/2 still retain modest positional separation even without PEs. This is likely due to architectural inductive biases, such as local windows in Swin, provide weak additional spatial anchoring. This aligns with the epipolar peak responses observed in the same models in Figure 1, reinforcing that certain inductive biases can sustain limited locality when positional information is removed.

B.4. PE-induced Kernel Visualization

We present visualization of PE-induced kernels here, as per the decomposition in Equation (5).

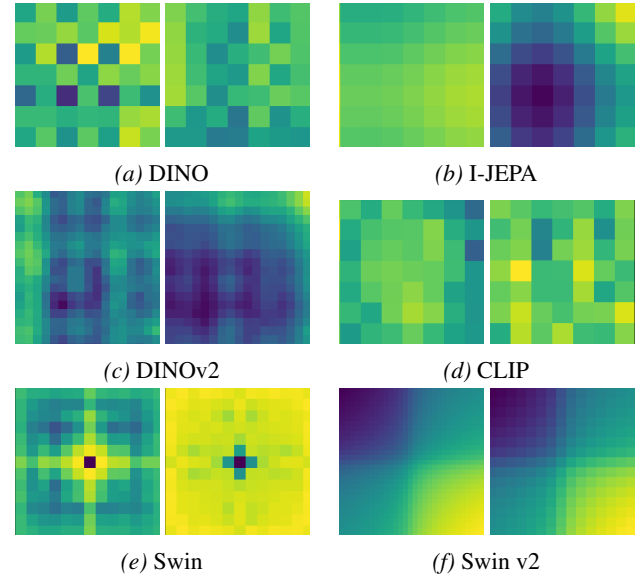


Figure 7. Visualization of PE-induced kernels. The left and right images are the the kernels from the first and last attention layers.

Table 6. Token-offset reconstruction. Each entry reports the cosine similarity between a reference token and its displaced neighbor token at offset k , in a *reconstruction/baseline* format. Without PEs, similarity becomes uniformly high across offsets, indicating that positional distinctiveness collapses.

	w/ PE			w/o PE		
	$k = 1$	$k = 2$	$k = 3$	$k = 1$	$k = 2$	$k = 3$
DINO	0.983/0.956	0.981/0.9334	0.980/0.917	0.981/0.970	0.979/0.965	0.979/0.962
DINOv2	0.722/0.606	0.692/0.573	0.670/0.472	0.909/0.879	0.902/0.858	0.900/0.618
DINOv3	0.762/0.688	0.713/0.549	0.689/0.468	0.998/0.996	0.998/0.996	0.998/0.996
IJEPA	0.912/0.664	0.915/0.537	0.919/0.427	0.998/0.998	0.998/0.997	0.998/0.998
DEiT	0.912/0.783	0.925/0.793	0.925/0.790	0.999/0.999	0.999/0.999	0.999/0.999
Siglip2	0.682/0.511	0.674/0.483	0.674/0.463	0.999/0.999	0.999/0.999	0.999/0.999
BeiT	0.999/0.999	0.999/0.999	0.999/0.999	0.999/0.999	0.999/0.999	0.999/0.999
Data2Vec	0.984/0.929	0.973/0.894	0.966/0.866	0.999/0.999	0.999/0.999	0.999/0.999
MLCD	0.734/0.551	0.719/0.521	0.722/0.500	0.769/0.638	0.761/0.609	0.759/0.594
VIT	0.875/0.710	0.875/0.631	0.862/0.624	0.999/0.999	0.999/0.999	0.999/0.999
SAM	0.994/0.987	0.992/0.984	0.990/0.984	0.998/0.996	0.996/0.995	0.995/0.993
CLIP	0.817/0.647	0.812/0.639	0.822/0.646	0.999/0.999	0.999/0.999	0.999/0.999
Swin	0.754/0.528	0.740/0.511	0.755/0.453	0.912/0.818	0.909/0.830	0.909/0.832
SwinV2	0.779/0.651	0.760/0.587	0.765/0.584	0.903/0.842	0.895/0.804	0.899/0.796

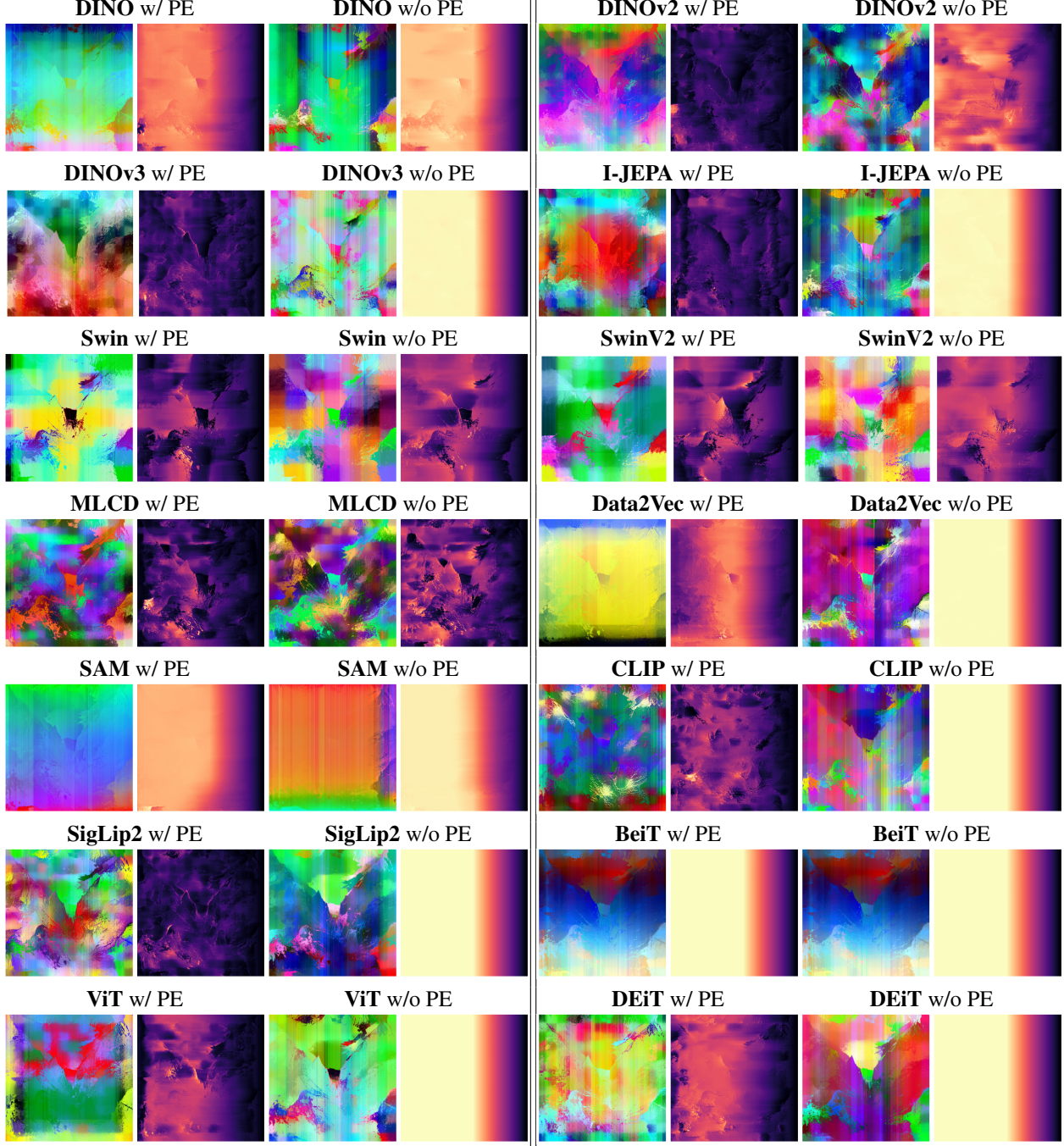


Figure 8. Visualization of the AnyUp interpolation of feature activations and their epipolar responses (left and right of each pair, respectively), shown with and without PE. With PE, models exhibit coherent spatial structure and well-localized epipolar responses. Removing PE consistently collapses both feature geometry and epipolar localization, manifesting as noisy patterns (DINO, Swin), stripe artifacts (Swin/SAM), or nearly blank activations (Data2Vec, MetaClip, SigLIP2).

Model	Bilinear			AnyUp		
	EPE↓	R@1↑	R@5↑	EPE↓	R@1↑	R@5↑
DINO	11.40	0.146	0.560	13.02	0.285	0.610
DINOv2	12.64	0.131	0.515	13.82	0.240	0.555
DINOv3	11.66	0.129	0.474	12.96	0.178	0.477
I-JEPA	9.90	0.151	0.561	10.98	0.259	0.587
DEiT	14.69	0.152	0.553	16.63	0.266	0.586
SigLIP2	11.04	0.141	0.519	11.33	0.221	0.544
BeiT	28.98	0.143	0.531	29.46	0.211	0.545
Data2Vec	17.55	0.153	0.564	24.56	0.256	0.588
MLCD	23.25	0.112	0.416	22.19	0.150	0.422
ViT	22.13	0.142	0.545	23.63	0.261	0.576
SAM	19.67	0.153	0.569	20.94	0.289	0.634
CLIP	21.39	0.148	0.531	21.40	0.232	0.538
Swin	30.87	0.087	0.331	32.82	0.082	0.274
SwinV2	27.53	0.095	0.360	30.17	0.096	0.305

(a) w/ PE

Model	Bilinear			AnyUp		
	EPE↓	R@1↑	R@5↑	EPE↓	R@1↑	R@5↑
DINO	24.21	0.126	0.477	26.68	0.174	0.471
DINOv2	38.08	0.087	0.315	38.00	0.099	0.296
DINOv3	51.89	0.080	0.293	51.32	0.088	0.264
I-JEPA	44.97	0.088	0.321	45.99	0.096	0.301
DEiT	26.22	0.122	0.436	27.53	0.149	0.411
SigLIP2	38.99	0.088	0.312	39.70	0.099	0.300
BeiT	46.31	0.115	0.441	48.13	0.145	0.415
Data2Vec	39.64	0.112	0.424	39.67	0.141	0.394
MLCD	38.36	0.086	0.314	38.43	0.096	0.289
ViT	28.36	0.110	0.414	29.29	0.136	0.387
SAM	47.07	0.156	0.574	45.73	0.292	0.644
CLIP	53.80	0.081	0.290	52.79	0.087	0.268
Swin	34.89	0.088	0.323	37.70	0.075	0.251
SwinV2	33.99	0.088	0.329	35.14	0.084	0.275

(b) w/o PE

Table 7. Comparison of different upsampling method for the stereo probing results at 448× resolution. We can see that the use of AnyUp will not affect EPE much (apart from Data2Vec), but can significantly improve the Recall performances.

B.5. Token-Level Epipolar Consistency

We present further evaluation results for the epipolar probing experiment as in Section 4.2. For each encoder, we extract low-resolution dense feature maps and upsample them to input resolution using two different strategies: (1) a standard **Bilinear** interpolation baseline, and (2) the adaptive **AnyUp** method (Wimmer et al., 2025), which learns content-aware upsampling filters that better preserve high-frequency structure and contextual cues. All models are evaluated at 448× resolution using our feature-level epipolar probe, with results summarized in Table 7. More visualizations are presented in Figure 8.

Results. With PE, models produce structured and spatially coherent feature maps. Their epipolar responses are sharply localized, indicating that positional information strongly constrains the spatial neighborhood over which tokens interact. This behavior is especially pronounced in DINO-series models, where the presence of PE yields clean, directional epipolar peaks that align with the underlying stereo geometry.

Removing PE leads to a dramatic collapse in geometric structure for nearly all models. Notably, aside of the epipolar response, removing PE can also significantly affect the feature space in DINO and SAM models. The MLCD model is the model unaffected models that preserves local features even without PE. In all other cases, the epipolar response becomes flat, diffuse, or completely uninformative, confirming that the geometry collapses when positional cues are removed.

AnyUp vs. Bilinear. Apart from Data2Vec, AnyUp does not affect the EPE for most models. AnyUp retains the underlying feature structure and enriches local semantics,

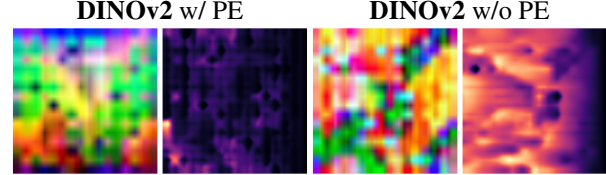


Figure 9. Visualization of the direct bilinear interpolation of feature activations and their epipolar responses (left and right of each pair, respectively), shown with and without PE. Visualizations are not semantically meaningful.

resulting in higher recall (R@1 and R@5) across most models. These improvements reflect that AnyUp can be used as a visualization tool that can preserve both the semantic distinctiveness without harming too much of the epipolar alignment of deep features. Figure 9 presents the direct bilinear interpolation of feature activations and their epipolar responses.

Shuffled PEs. In addition, we provide qualitative results of epipolar responses under random and pairwise PE shuffling in Figure 10. Combining with the quantitative results in our main paper, though pairwise PE for absolute encoding schemes preserve geometry correspondence, the visualizations present in a chaotic manner that are not visually interpretable.

The BEiT exception. BEiT stands out as an outlier, failing to exhibit any geometric correspondence even without any PE altering. This aligns with prior observations that BEiT produces smooth, low-frequency representations with limited spatial specificity (Bao et al., 2022; He et al., 2022; Oquab et al., 2024; El Banani et al., 2024). Interestingly, Data2Vec maintains stronger correspondence, despite

When Positional Embeddings Help and Hurt Spatial Reasoning

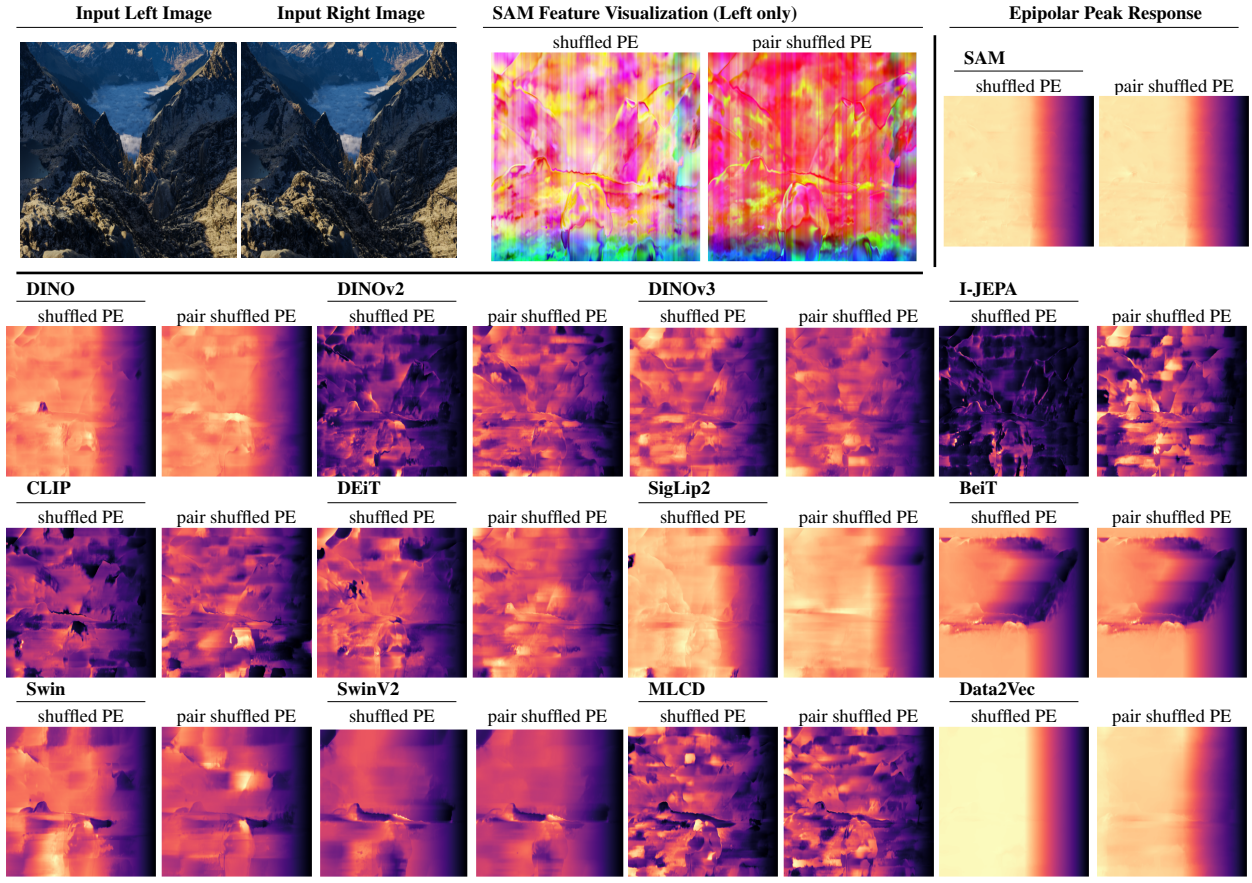


Figure 10. **Epipolar peak response visualization for shuffled PEs.** Top-left: an example stereo pair and the corresponding SAM feature maps with and without paired PE shuffling. Shuffled PEs result in collapsed/uninterpretable peak correspondence in general.

employing the same positional encoding strategy as BEiT. Since BEiT predicts discrete visual tokens via a dVAE, while Data2Vec predicts continuous latent representations, this suggests that discretization or quantization may suppress fine-grained geometry. We emphasize, however, that disentangling the precise roles of discretization and quantization in shaping geometric fidelity remains an open question.

Residual Positional Cues. Interestingly, several architectures (*e.g.*, Swin, MLCD) preserve a degree of spatial structure even when PEs are removed. This residual locality is likely induced by the architectural design (*e.g.*, local windows, multi-scale hierarchies) that implicitly encode spatial structure. Understanding these implicit sources of spatial structure and how they interact with or complement explicit positional encodings also poses an interesting direction for future architecture design.